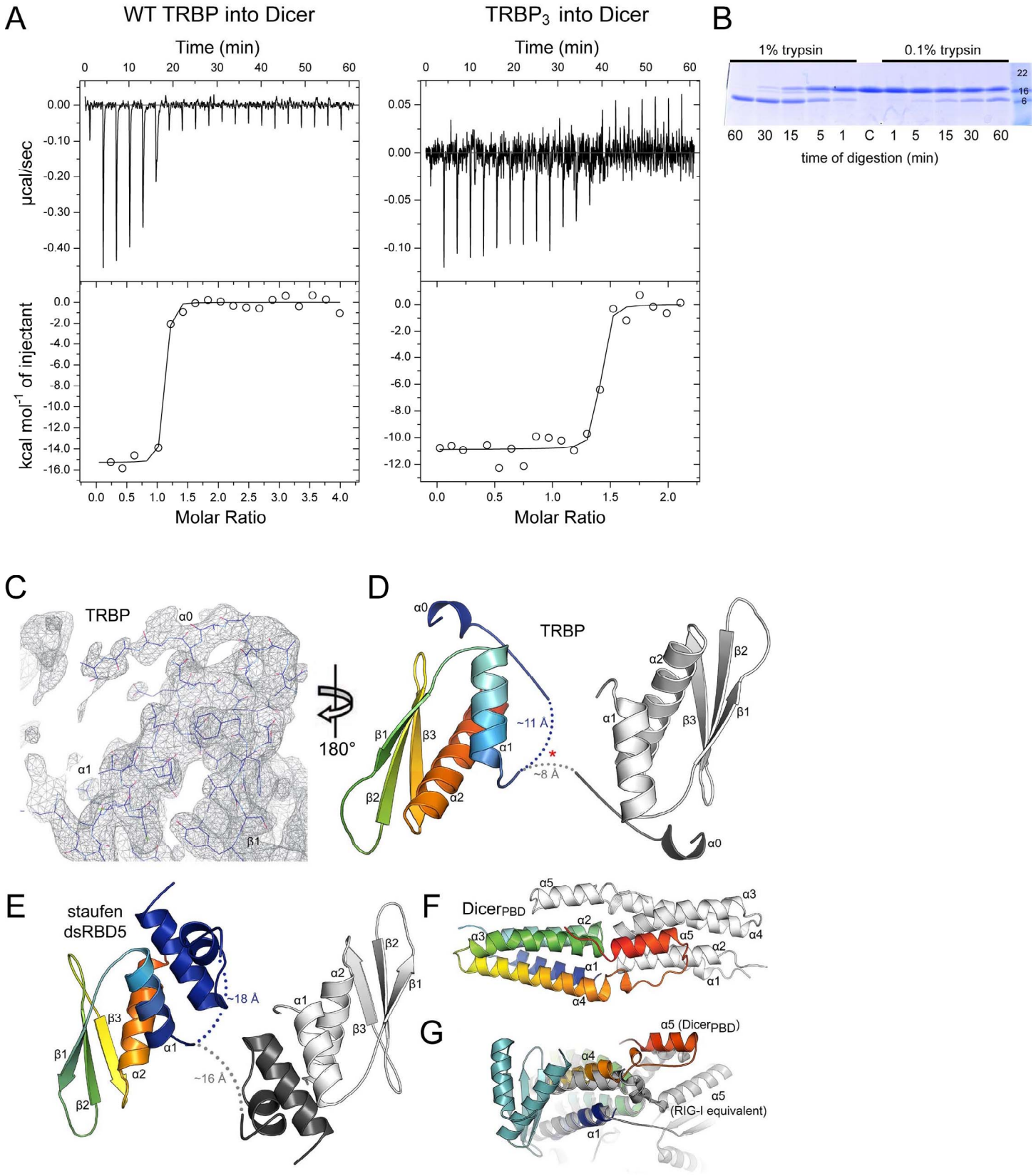

Figure S1, related to main figure 1. TRBP and Dicer: structure and interactions. (A) Thermograms resulting from titration of WT TRBP (left) or $TRBP_3$ (right) into Dicer. Duplicate runs yielded the following values for WT TRBP: K_d = 2.8 ± 1.7 nM, ΔH = -15.9 ± 0.48 kcal/mol, n = 0.84 ± 0.013; $TRBP_3$: K_d = 4.3 ± 2.5 nM, ΔH = -23.2 ± 1.3 kcal/mol, n = 1.35 ± 0.025. Stoichiometric deviations from n=1 likely result from protein samples that are partially misfolded, aggregated, or otherwise incompetent for binding. (B) Trypsin digestion of human TRBP residues 228–366 (dsRBD3 plus the 70 residues between it and dsRBD2) reveals the stable $TRBP_3$ core

(residues 258–366) used for crystallography. This corresponds to a globular domain ~50% larger than a typical dsRBD. Protein marker ladder is labeled with kDa values. (C) An omit map contoured at 1.0 σ showing unbiased density for the partially helical portion of $TRBP_3$ (α0) N-terminal of the dsRBD fold. (D) The canonical dsRBD fold consists of α1, β1, β2, β3, and α2. Orientation of adjacent $TRBP_3$ protomers in the crystal reveals the possibilty of domain-swapping involving the 36 amino acid extension N-terminal to the dsRBD fold. Disorder prevents assignment of the fold as *cis* (~11 Å distance) or *trans* (~8 Å distance). It is plausible that the domain-swapped *trans* conformation is adopted above the 54 μM K_d observed for TRBP dimerization, while the *cis* conformation is adopted when the protein is a monomer. A red asterisk marks the approximate location of two phosphorylation sites (S283, S286) found within a linker region disordered in the crystal. (E) Staufen (PDB ID: 4DKK)(Gleghorn et al., 2013) contains a non-canonical dsRBD with a 1.9 Å backbone root-mean-square deviation to the non-canonical dsRBD found in $TRBP_3$. Staufen contains an N-terminal extension involved in domain swapping. (F) Crystal contacts between neighboring copies of $Dicer_{PBD}$, mediated by helix α5 and the preceding loop. (G) Homodimeric contacts between Dicer protomers are not likely to be biologically relevant. For the dimer to form, helix α5 must adopt a conformation inconsistent with the fold of its natural helicase context, as demonstrated by alignment to the structure of homologous helicase RIG-I (PDB ID: 4AY2)(Luo et al., 2012).

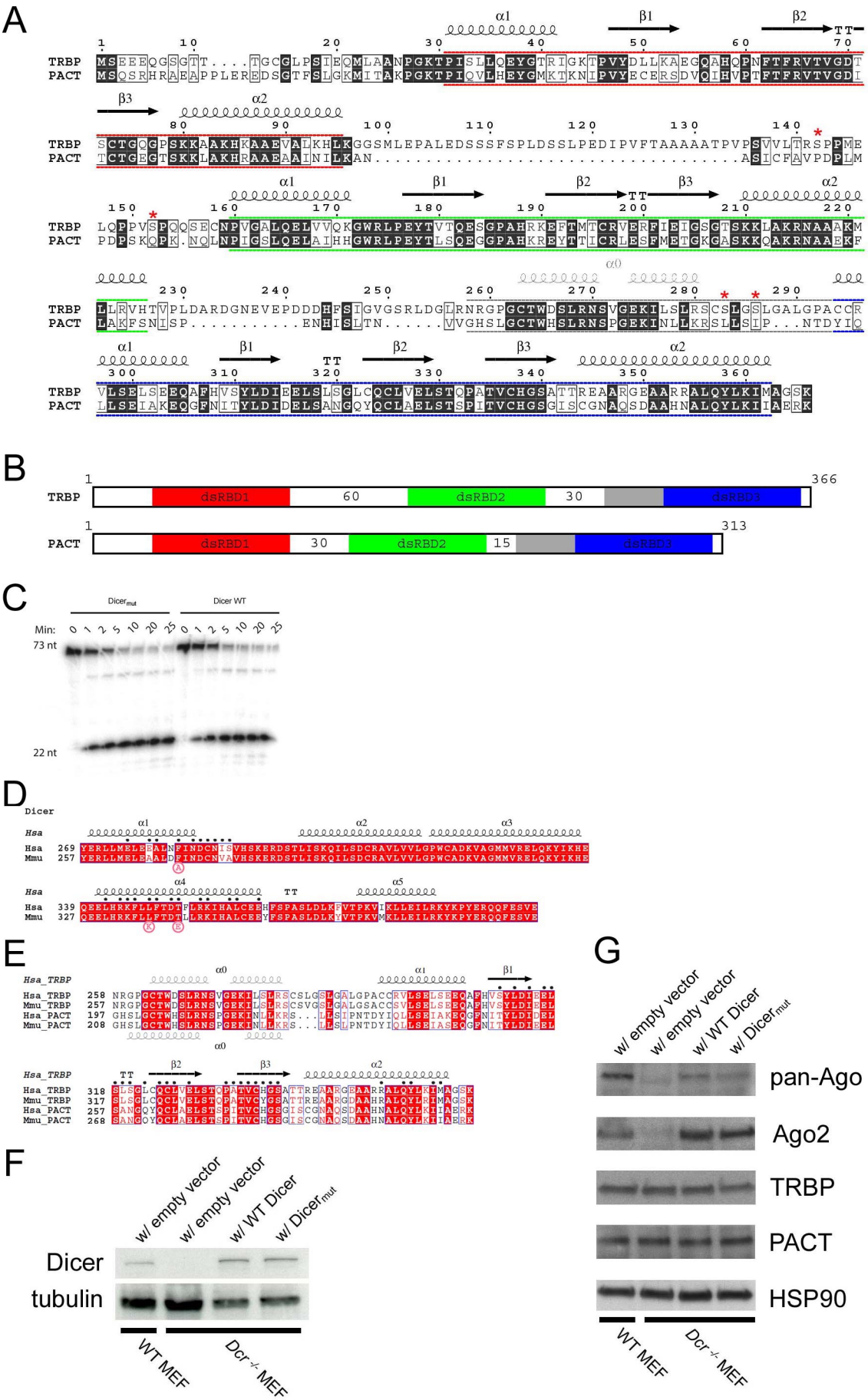

Figure S2, related to main figure 2. Sequences of TRBP and PACT, and mutation of Dicer. (A) Domain structure and conservation of TRBP and PACT. The dsRBDs are marked by red, green, or blue for the first,

second, or third domains, respectively. The structured extension N-terminal to dsRBD3 is shown in grey.Sequence alignment of human TRBP and PACT. Secondary structure elements from independently reported TRBP domain structures (PDB ID: dsRBD 1, 3LLH; dsRBD 2, 2CPN)(Yamashita et al., 2010) or from the present crystal structure (dsRBD3) are shown above the sequences. Labels for potential α0 helices outside the canonical dsRBD region are based on a prediction from the Jpred server. The globular $TRBP_3$ domain (grey, blue regions) is defined based on mass spectrometric analysis following trypsin digestion. Notably, trypsin cleaved after arginine 257, less efficiently after arginine 259, and not detectably after arginine 269, providing precision in the domain assignment. Red asterisks mark known TRBP phosphorylation sites. (B) Scale representation of the domain structure in TRBP and PACT. Inset numbers represent the estimated length of flexible linkers. Based on conservation and secondary structure prediction, PACT is expected to feature a structured region in the linker between the second and third domains analogous to the one observed in TRBP. (C) Cleavage assay demonstrating indistinguishable pre-let-7 dicing activity of $Dicer_{mut}$ and WT Dicer. (D) $Dicer_{PBD}$ alignment between human and mouse; secondary structure observed in the crystal structure is indicated above the aligned sequences. Interfacial TRBP or Dicer residues found within 5 Å of the binding partner are indicated with a black dot. Alignment of the human $Dicer_{PBD}$ domain residues used in crystallization vs. the equivalent mouse residues. Pink letters indicate the three Dicer mutations used to abrogate binding to TRBP or PACT. (E) Alignment of $TRBP_3$ and the equivalent region in PACT between human and mouse; secondary structure observed for TRBP in the crystal structure is indicated above the aligned sequences. Cartoons marking likely α0 helices outside the canonical dsRBD region are based on predictions from the Jpred server. (F) Western blot demonstrating comparable levels of Dicer in transfected (rescue) conditions and in WT MEF cells. This also confirms the absence of Dicer in the *Dcr*$^{-/-}$ MEF line. (G) Western blots for Ago proteins (the pan-Ago antibody detects Ago1/Ago2/Ago3/Ago4), TRBP, and PACT under various experimental conditions. Ago levels are dependent on the presence of Dicer, while TRBP and PACT levels are generally independent of Dicer/Ago levels.

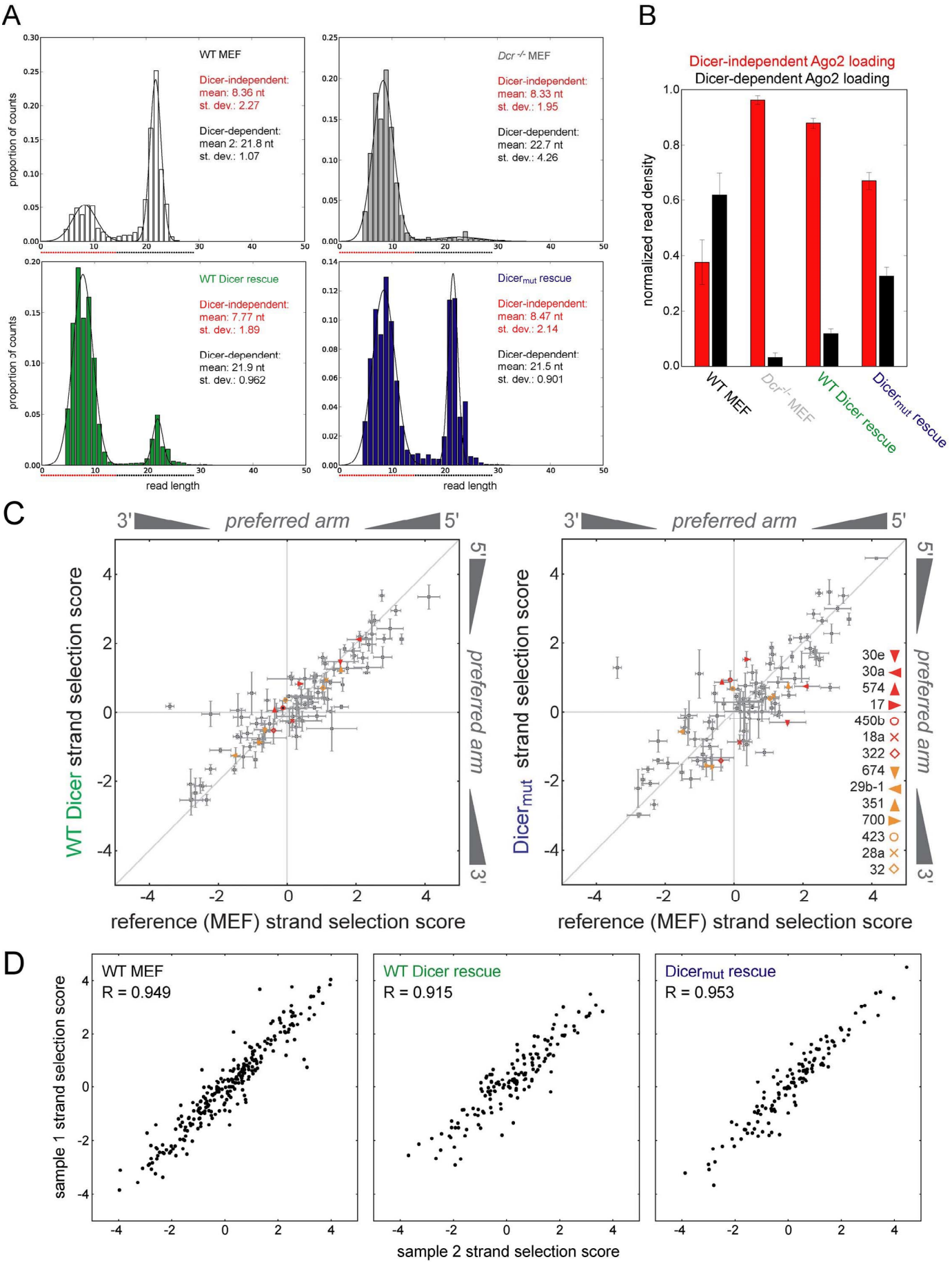

Figure S3, related to main figure 3. (continues)

Figure S3, related to main figure 3. (continued)

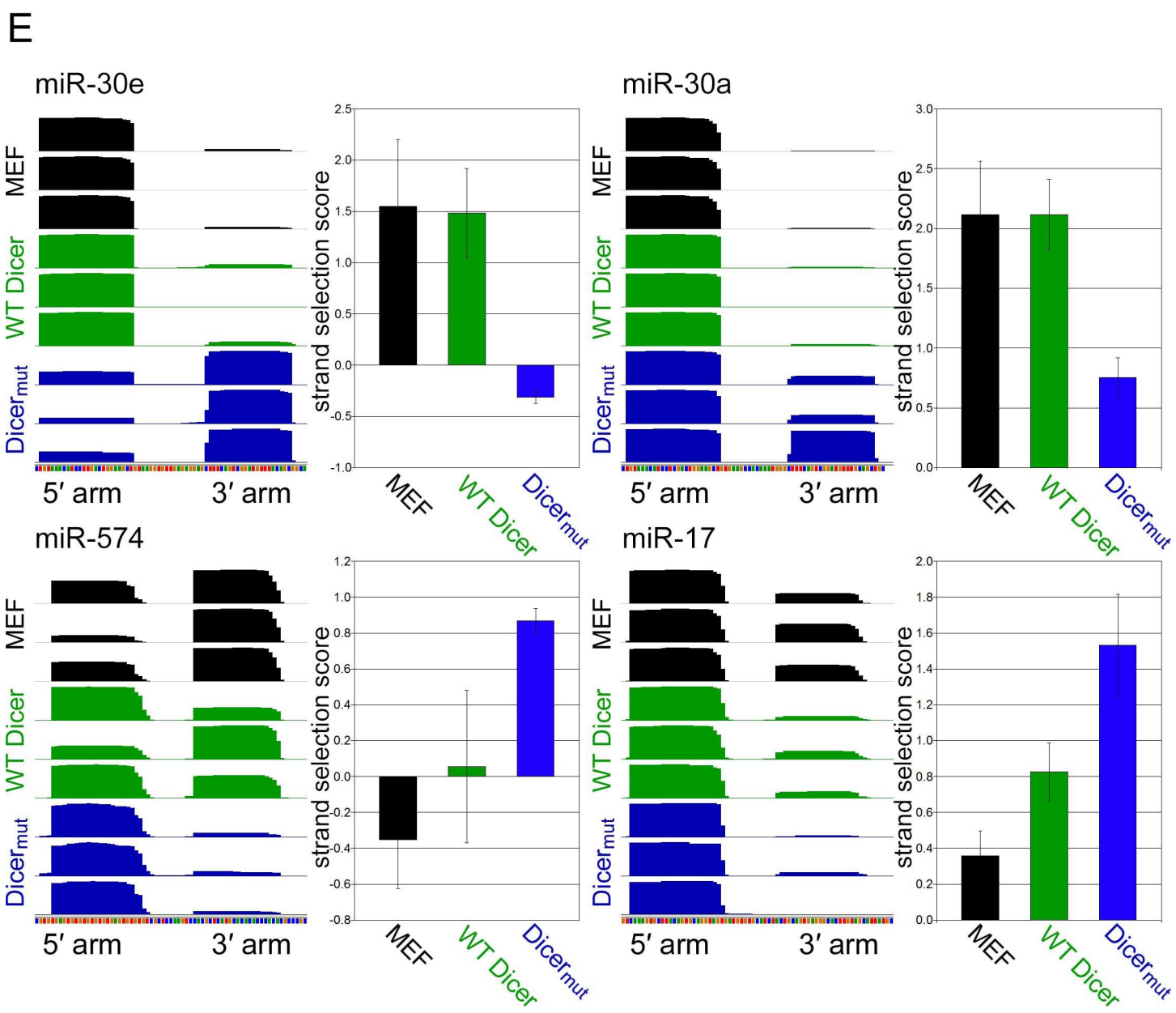

Figure S3, related to main figure 3. RNA sequencing data. (A) Histogram plots of normalized read coverage versus length for Ago2-coimmunoprecipitated RNA in WT MEF cells, *Dcr*$^{-/-}$ MEF, *Dcr*$^{-/-}$ MEF rescued with WT Dicer, and *Dcr*$^{-/-}$ MEF rescued with Dicer$_{mut}$. Two distinct populations are observed: shorter reads (mean ≈ 8 nt) are associated with Dicer-independent Ago2 loading while longer reads (mean ≈ 22 nt) are associated with canonical, Dicer-dependent miRNA processing. (B) Quantification of read density for Dicer-independent (< 15 nt RNA) and Dicer-dependent (≥ 15 nt RNA) loading of Ago2 demonstrates that canonical loading of Argonaute is not assisted by the presence of TRBP and PACT. Each data point represents an average value ±SD from biological triplicates. Rescue conditions are not able to recover fully to the typical ratio between the two pools of miRNA length during the 24 h following transfection, likely due to the extremely long (~1 week) half-life of Ago2 (Nabanita et al., 2013). (C) Strand selection data showing error bars from three biological replicates. Correlation of strand selection behavior (scored as log(5′ arm coverage / 3′ arm coverage)) between WT MEF (X axis) and rescue conditions (Y axis) with either WT Dicer or Dicer$_{mut}$ demonstrates the importance of TRBP and PACT in maintaining fidelity of strand selection. In the Dicer$_{mut}$ condition, an increased deviation from the diagonal is observed due to impaired ;strand selection fidelity. Labels denote the miRNA duplexes most dramatically affected. Duplexes varying by more than one standard deviation between MEF and WT

rescue conditions are not considered based on the likelihood that they are behaving aberrantly due to use of the Dicer-KO cell line. (D) Paired correlations between biological replicate samples for three conditions demonstrates reproducibility of strand selection observations. Strand selection score is defined as: log⟨5′ arm coverage / 3′ arm coverage⟩. Similar behavior is observed between replicates. These plots include more points than the plots comparing between conditions (Fig. 3A) because those cases require that qualifying counts be present in all of the conditions being compared. (E) Deep sequencing coverage for the 5′ and 3′ arms of four miRNA duplexes where Dicer protein partners TRBP and PACT contribute most to the fidelity of strand selection. Biological triplicate results for WT MEF, WT Dicer rescue, and $Dicer_{mut}$ rescue are shown in black, green, and blue, respectively. Inset plots show quantified strand selection scores (defined as log⟨5′ arm coverage / 3′ arm coverage⟩) by sample. Each data point represents an average value ±SD from replicates. WT Dicer rescue (green) traces approximate strand selection behavior of WT MEF cells (black), while $Dicer_{mut}$ rescue (blue) traces deviate from the traditional strand selection behavior.

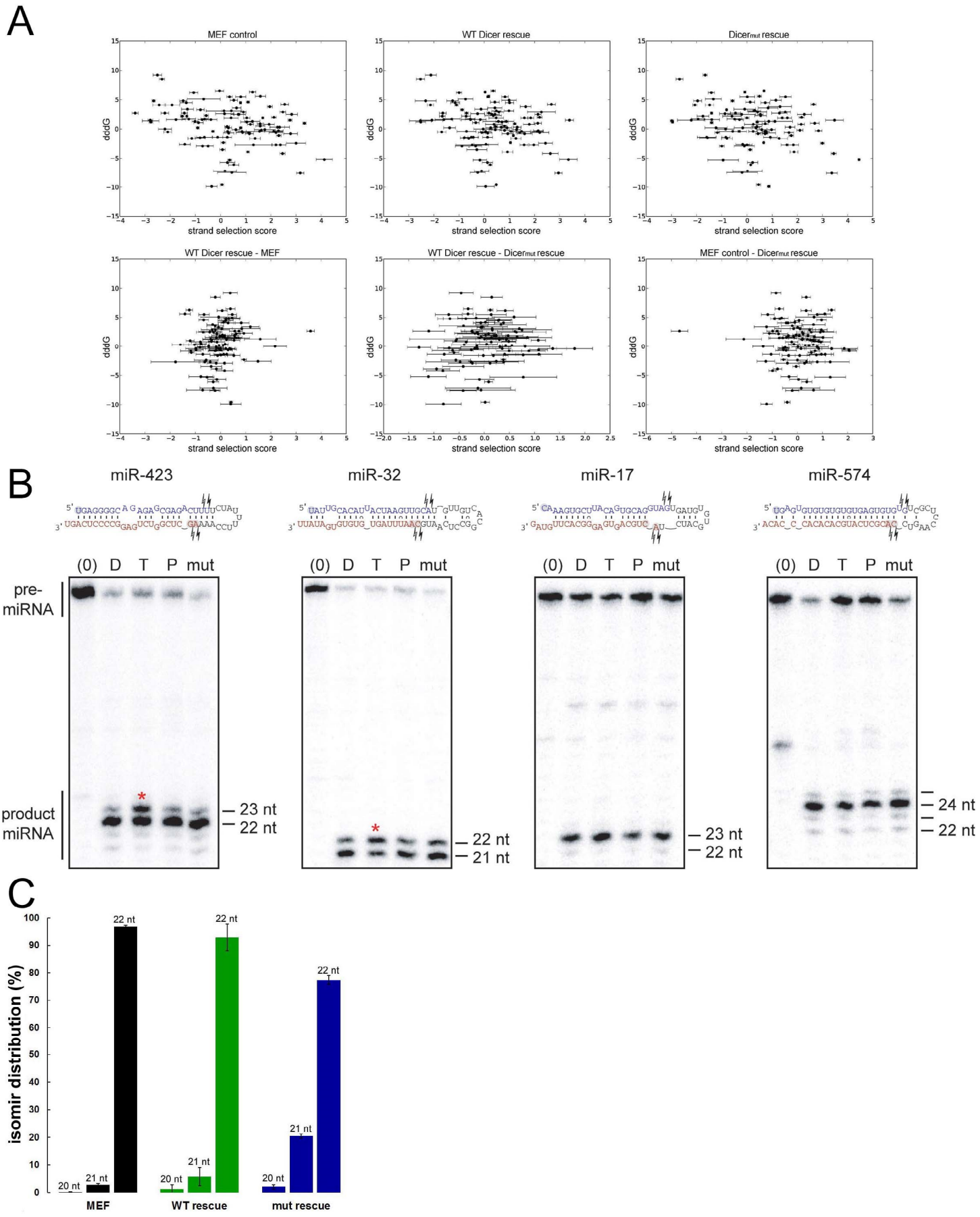

Figure S4, related to main figure 4. RNA sequencing and biochemical data. (A) Assessment of thermodynamic asymmetry in miRNA duplexes as correlated to the strand selection score (log⟨5p arm coverage

/ 3p arm coverage⟩). The top row of plots compares each observed strand selection score to the difference in calculated thermodynamic stability between the two termini of a miRNA duplex. A positive dddG value corresponds to greater stability at the 5′ end of the 5p arm. Using a Pearson R test for correlation, none of these correlations are significant; correlation in all cases is between -0.3 and +0.3. (B) *In vitro* dicing assay for miR length. Lanes show uncleaved pre-miR, cleavage with Dicer alone, Dicer plus TRBP, Dicer plus PACT, or $Dicer_{mut}$ alone. For pre-miR-423 and pre-miR-32, the cleavage position is influenced by the presence of TRBP (asterisk) but is insensitive to PACT, while the other two pre-miRNAs assayed are insensitive to dsRBPs. Secondary structures of pre-miR substrates are shown, with filled or open icons respectively representing the typical or variant Dicer cleavage positions. Grey circles represent potential resulting 5′ termini of the miRNA duplex. (C) Distribution of length variants in the predominant, 3p arm of miR-132 under different experimental conditions. Values are by percentage of the total reads for 20, 21, and 22 nt RNAs. Error bars represent the standard deviation between three replicates. 21 nt isomiRs become more abundant when Dicer cannot recruit TRBP/PACT.

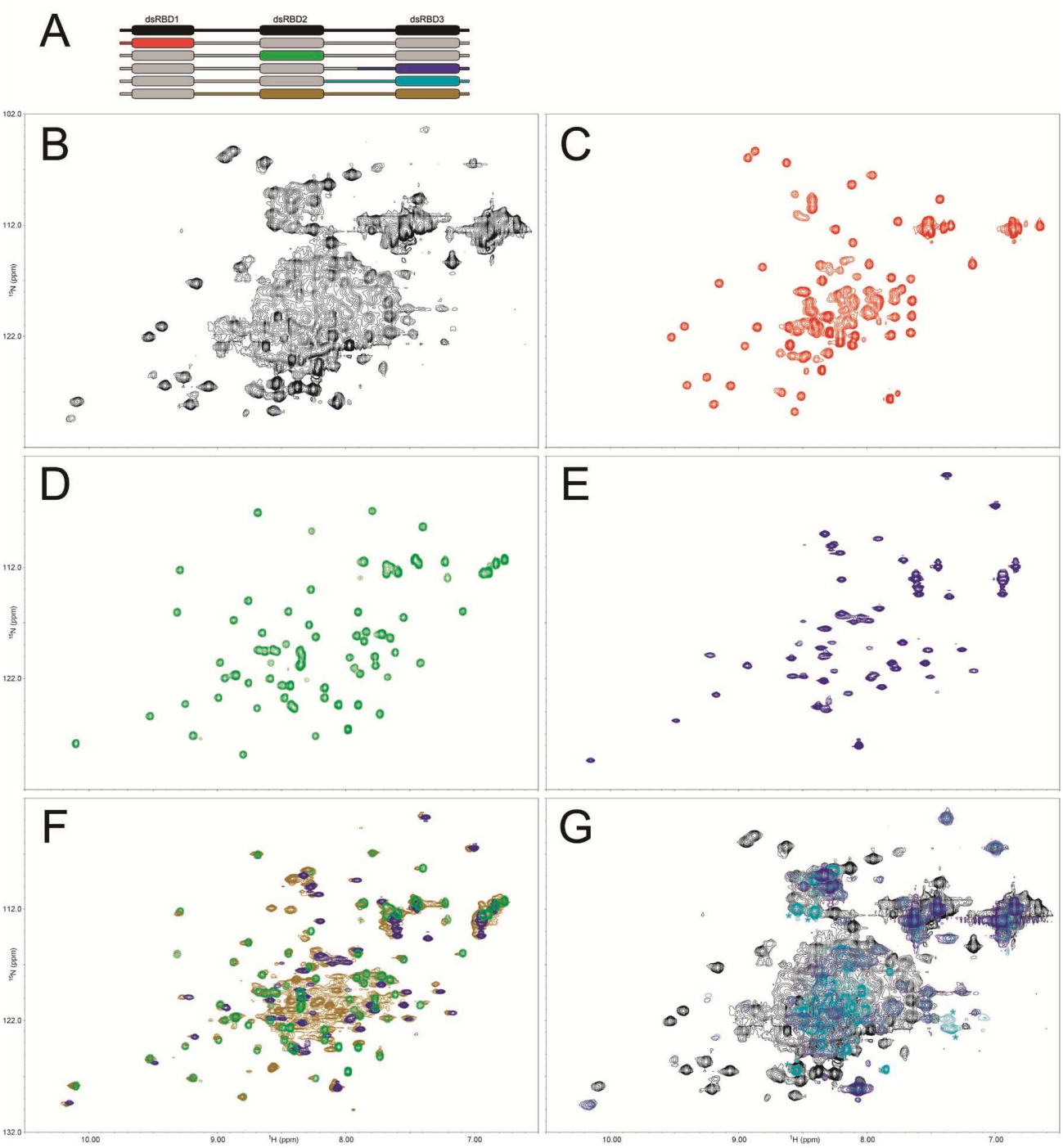

Figure S5, related to main figure 5. ^{1}H-^{15}N HSQC spectra of TRBP domains. (A) Legend for the different domains used. Black, wild type; red, dsRBD1; green, dsRBD2; blue, dsRBD3 with the preceding 36 residues ($TRBP_3$); teal, dsRBD3 with the preceding 67 residues; brown, dsRBD2 and dsRBD3 with the linker residues N-terminal to each domain. (B) Spectrum of the full length (wild type) TRBP with all domains contained in a single polypeptide (1 mM). (C) Spectrum of dsRBD1 (1 mM). (D) Spectrum of dsRBD2 (1 mM). (E) Spectrum of dsRBD3 with the preceding 36 residues ($TRBP_3$, 138 μM). (F) Overlaid spectra of dsRBD2 (green, 1 mM), $TRBP_3$ (blue, 138 μM), and the construct containing both domains plus the additional linker residues (brown, 116 μM). This demonstrates that dsRBD2 peaks are not perturbed in the context of dsRBD3 and the intervening linker. It has previously been shown that dsRBD2 does not interact with dsRBD1 in the absence of binding partners(Benoit et al., 2013). (G) Overlaid spectra of wild type TRBP (black, 1 mM), $TRBP_3$ (blue, 1 mM), and dsRBD3 with the preceding 67 residues (teal, 1 mM). Asterisks mark prominent peaks (not accounted for in the context of Figure 4) corresponding to residues found in the 31 residue linker N-terminal to $TRBP_3$.

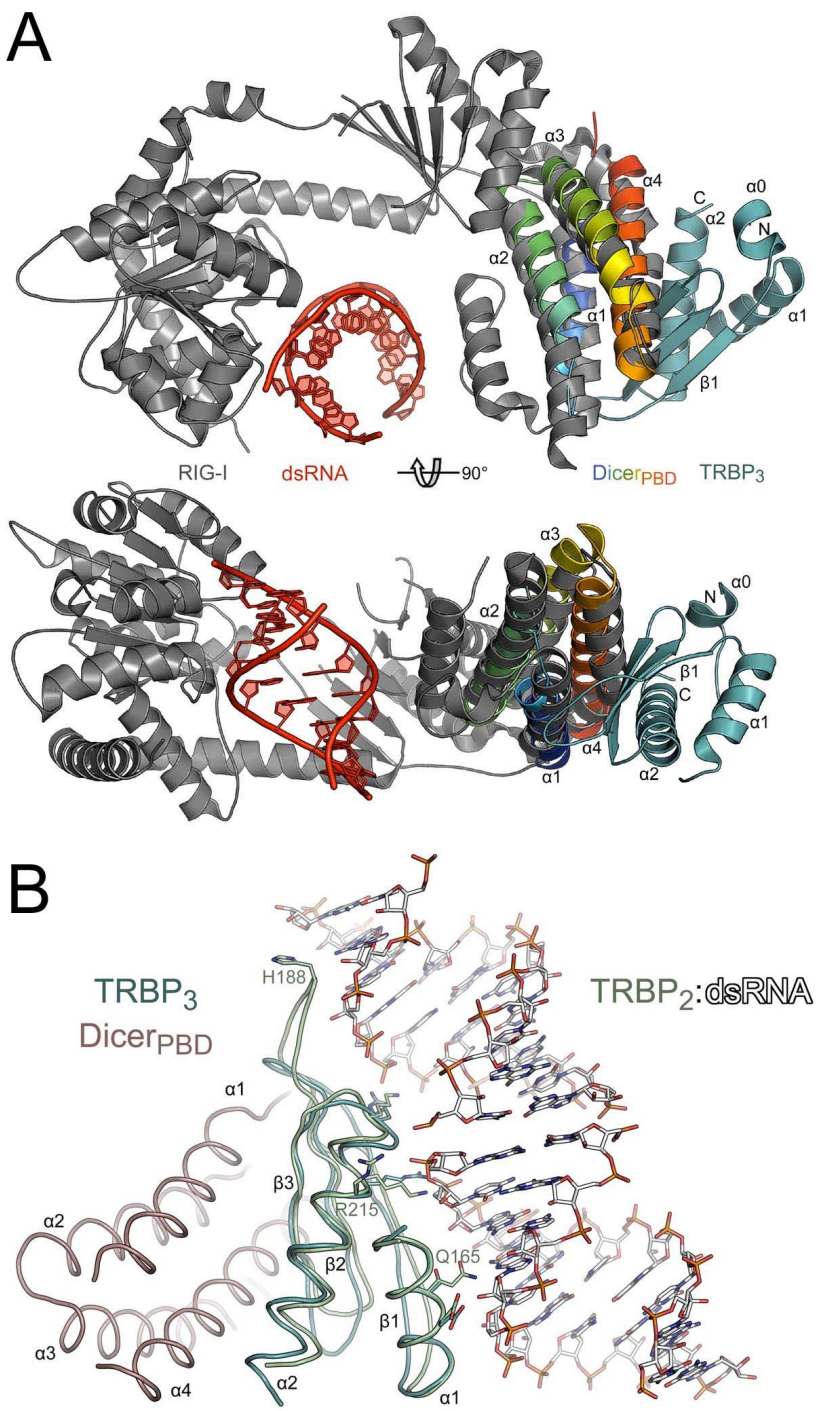

Figure S6, related to main figure 6. Comparison of domains in the Dicer:TRBP interface structure. (A) Structural similarity between the $Dicer_{PBD}$ and the equivalent portion of the helicase RIG-I (PDB ID: 4AY2)(Luo et al., 2012). The RIG-I structure (grey) contains a dsRNA duplex (red). In the likely case that Dicer's helicase adopts a tertiary structure similar to that of RIG-I, TRBP will rest on the outside of the helicase "clamp" that binds dsRNA. In the bottom view, the N-terminus extends "up" from α0, in the same direction that the Dicer architecture extends with its paired RNase III domains and its PAZ domain. (B) The dsRBD architecture is conserved between the second and third domains of TRBP, but different faces of the domain are utilized in binding. $TRBP_3$ (cyan) binds to $Dicer_{PBD}$ using a face distinct from that used by $TRBP_2$ (green, PDB ID: 3ADL)(Yang et al., 2010) to bind dsRNA. $TRBP_2$ residues involved in RNA recognition are shown as sticks, as are the $TRBP_3$ residues in equivalent positions (except in the case of glycine or a shortened loop). $TRBP_3$ bears dissimilar features in positions corresponding to $TRBP_2$ residues Q165, H188, and R215, contributing to the domain's loss of dsRNA affinity.

Table S1, related to main figure 3. Relative abundance of the miRNAs most different between the $Dcr^{-/-}$ rescue conditions using WT Dicer or $Dicer_{mut}$. The "%" value refers to the share of reads for a given miRNA for a particular replicate, and the standard deviation is reported for that value between three replicates. The "Total%" value demonstrates that the majority of the Ago2-bound miRNAs in the $Dicer_{mut}$ condition correspond to one of these eight miRNAs.

	MEF		**WT rescue**		**mut rescue**		
miR	%	stdev	%	stdev	%	stdev	mut/WT ratio
99b	8.7	39	5.9	30	16.3	4	2.8
342	0.4	36	1.0	42	2.1	25	2.2
10b	0.6	39	6.7	29	11.4	20	1.7
99a	3.1	19	12.3	18	19.7	32	1.6
23a	4.5	31	2.6	7	4.1	33	1.5
let7f-2	2.6	15	0.1	84	0.2	39	1.5
100	0.7	53	0.4	34	0.5	11	1.5
125a	3.0	22	4.3	14	5.6	28	1.3
Total %	23.5		33.2		59.8		

Table S2, related to main figure 3. The spreadsheet lists strand selection scores (log⟨5p arm coverage / 3p arm coverage⟩) for the 108 microRNAs that could be compared across MEF, WT Dicer rescue, and $Dicer_{mut}$ rescue conditions. Scores are reported for three biological replicates and as an averaged value with standard deviation.

Table S3, related to main figure 3. MicroRNAs whose strand selection behavior is dramatically altered in the absence of Dicer partner dsRBPs. Human miR equivalent are noted in parentheses when homolog naming differs from mouse miR. The "Δs.s." values denote the change in strand selection score (defined as log⟨5′ arm coverage / 3′ arm coverage⟩) between the WT MEF reference sample and the $Dicer_{mut}$ sample.

miRNA	**Δs.s.**	**Association**	**Reference**
30e	1.87	breast cancer	(Ouzounova et al., 2013)
30a	1.36	breast cancer	(Zeng et al., 2013)
574	1.22	colorectal cancer	(Ji et al., 2013)
17	1.17	proliferation	(Olive et al., 2013)
450b	1.34	eye development	(Shalom-Feuerstein et al., 2012)
18a	1.23	DNA damage response	(Song et al., 2011)
322 (424)	1.41	differentiation	(Sarkar et al., 2010)
674	0.96	Huntington's disease	(Lee et al., 2011)
29b-1	0.91	Alzheimer's	(Hebert et al., 2008)
351	0.85	differentiation	(Li et al., 2012)
700	0.76	unknown; absent in humans	-
423	0.71	cell proliferation	(Lin et al., 2011)
28a	0.71	leukemia	(Girardot et al., 2010)
32	0.64	colorectal cancer	(Wu et al., 2013)

Table S4, related to main figure 3. Sequencing reads throughout data processing and analysis. Note that total input RNA was normalized before library preparation, so the "input" values do not reflect the amount of RNA obtained via Ago2 immunoprecipitation under the various experimental conditions.

sample	**MEF**			**Dcr$^{-/-}$**		
replicate	1	2	3	1	2	3
input	4.7×10^7	6.1×10^7	5.5×10^7	5.0×10^7	5.0×10^7	5.4×10^7
clipped	1.5×10^7	1.5×10^7	1.8×10^7	2.0×10^7	1.5×10^7	1.7×10^7
collapsed	1.1×10^7	1.1×10^7	1.2×10^7	1.6×10^7	1.3×10^7	1.1×10^7
	alignment			*alignment*		
unaligned	2.6×10^6	2.5×106	3.4×10^6	6.5×10^6	7.2×10^6	4.1×10^6
unique	3.3×10^6	2.6×106	3.6×10^6	1.2×10^6	1.0×10^6	8.1×10^5
ambigious	5.1×10^6	6.3×106	5.2×10^6	8.1×10^6	5.1×10^6	6.1×10^6
pseudoreads	8.4×10^6	8.9×106	8.8×10^6	9.2×10^6	6.1×10^6	6.9×10^6
% aligned	77%	78%	72%	59%	46%	63%

sample	**WT rescue**			**mut rescue**		
replicate	1	2	3	1	2	3
input	5.0×10^7	5.6×10^7	5.3×10^7	6.4×10^7	6.8×10^7	4.1×10^7
clipped	1.8×10^7	1.1×10^7	1.4×10^7	1.6×10^7	1.7×10^7	2.0×10^7
collapsed	1.5×10^7	4.7×10^6	1.3×10^7	1.2×10^7	1.2×10^7	1.4×10^7
	alignment			*alignment*		
unaligned	4.3×10^6	1.3×10^6	5.5×10^6	5.3×10^6	6.4×10^6	4.7×10^6
unique	1.7×10^6	4.0×10^5	2.1×10^6	1.8×10^6	1.8×10^6	1.6×10^6
ambigious	8.6×10^6	3.1×10^6	5.2×10^6	4.5×10^6	3.5×10^6	7.9×10^6
pseudoreads	1.0×10^7	3.5×10^6	7.4×10^6	6.3×10^6	5.3×10^6	9.5×10^6
% aligned	71%	73%	57%	54%	45%	67%

References for Supplemental Information

Benoit, M., Imbert, L., Palencia, A., Pérard, J., Ebel, C., Boisbouvier, J., and Plevin, M. (2013). The RNA-binding region of human TRBP interacts with microRNA precursors through two independent domains. Nucleic Acids Research *41*, 4241-52.

Girardot, M., Pecquet, C., Boukour, S., Knoops, L., Ferrant, A., Vainchenker, W., Giraudier, S., and Constantinescu, S. (2010). miR-28 is a thrombopoietin receptor targeting microRNA detected in a fraction of myeloproliferative neoplasm patient platelets. Blood *116*, 437-445.

Gleghorn, M., Gong, C., Kielkopf, C., and Maquat, L. (2013). Staufen1 dimerizes through a conserved motif and a degenerate dsRNA-binding domain to promote mRNA decay. Nature Structural &Amp; Molecular Biology *20*, 515-24.

Hebert, S., Horre, K., Nicolai, L., Papadopoulou, A., Mandemakers, W., Silahtaroglu, A., Kauppinen, S., Delacourte, A., and Strooper, B. (2008). Loss of microRNA cluster miR-29a/b-1 in sporadic Alzheimer's disease correlates with increased BACE1/ -secretase expression. Proceedings Of The National Academy Of Sciences *105*, 6415-6420.

Ji, S., Ye, G., Zhang, J., Wang, L., Wang, T., Wang, Z., Zhang, T., Wang, G., Guo, Z., Luo, Y., et al. (2013). miR-574-5p negatively regulates Qki6/7 to impact -catenin/Wnt signalling and the development of colorectal cancer. Gut *62*, 716-726.

Lee, S., Chu, K., Im, W., Yoon, H., Im, J., Park, J., Park, K., Jung, K., Lee, S., Kim, M., et al. (2011). Altered microRNA regulation in Huntington's disease models. Experimental Neurology *227*, 172-179.

Li, X., Feng, R., Huang, C., Wang, H., Wang, J., Zhang, Z., Yan, H., and Wen, T. (2012). MicroRNA-351 regulates TMEM 59 (DCF1) expression and mediates neural stem cell morphogenesis. RNA Biology *9*, 292-301.

Lin, J., Huang, S., Wu, S., Ding, J., Zhao, Y., Liang, L., Tian, Q., Zha, R., Zhan, R., and He, X. (2011). MicroRNA-423 promotes cell growth and regulates G1/S transition by targeting p21Cip1/Waf1 in hepatocellular carcinoma. Carcinogenesis *32*, 1641-1647.

Luo, D., Kohlway, A., Vela, A., and Pyle, A. (2012). Visualizing the determinants of viral RNA recognition by innate immune sensor RIG-I. Structure (London, England : 1993) *20*, 1983-8.

Nabanita, Young, L., Lau, P., Meisner, N., Morrissey, D., and MacRae, I. (2013). Highly complementary target RNAs promote release of guide RNAs from human Argonaute2. Molecular Cell *50*, 344-55.

Olive, V., Li, Q., and He, L. (2013). mir-17-92: a polycistronic oncomir with pleiotropic functions. Immunological Reviews *253*, 158-166.

Ouzounova, M., Vuong, T., Ancey, P., Ferrand, M., Durand, G., Kelm, F., Croce, C., Matar, C., Herceg, Z., and Hernandez-Vargas, H. (2013). MicroRNA miR-30 family regulates non-attachment growth of breast cancer cells. BMC Genomics *14*, 139.

Sarkar, S., Dey, B., and Dutta, A. (2010). MiR-322/424 and -503 Are Induced during Muscle Differentiation and Promote Cell Cycle Quiescence and Differentiation by Down-Regulation of Cdc25A. Molecular Biology Of The Cell *21*, 2138-2149.

Shalom-Feuerstein, R., Serror, L., Divonne, S., Petit, I., Aberdam, E., Camargo, L., Damour, O., Vigouroux, C., Solomon, A., Gaggioli, C., et al. (2012). Pluripotent Stem Cell Model Reveals Essential Roles for miR-450b-5p and miR-184 in Embryonic Corneal Lineage Specification. STEM CELLS *30*, 898-909.

Song, L., Lin, C., Wu, Z., Gong, H., Zeng, Y., Wu, J., Li, M., and Li, J. (2011). miR-18a Impairs DNA Damage Response through Downregulation of Ataxia Telangiectasia Mutated (ATM) Kinase. Plos ONE *6*, e25454.

Wu, W., Yang, J., Feng, X., Wang, H., Ye, S., Yang, P., Tan, W., Wei, G., and Zhou, Y. (2013). MicroRNA-32 (miR-32) regulates phosphatase and tensin homologue (PTEN) expression and promotes growth, migration, and invasion in colorectal carcinoma cells. Molecular Cancer *12*, 30.

Yamashita, S., Nagata, T., Kawazoe, M., Takemoto, C., Kigawa, T., Güntert, P., Kobayashi, N., Terada, T., Shirouzu, M., Wakiyama, M., et al. (2010). Structures of the first and second double-stranded RNA-binding domains of human TAR RNA-binding protein. Protein Science *20*, 118-130.

Yang, S.W., Chen, H., Yang, J., Machida, S., Chua, N., and Yuan, Y.A. (2010). Structure of Arabidopsis HYPONASTIC LEAVES1 and Its Molecular Implications for miRNA Processing. Structure/Folding And Design *18*, 594-605.

Zeng, R., Zhang, W., Yan, X., Ye, Z., Chen, E., Huang, D., Zhang, X., and Huang, G. (2013). Down-regulation of miRNA-30a in human plasma is a novel marker for breast cancer. Medical Oncology *30*.